








RESEARCH ARTICLE

Structural and Raman study of the thermoelectric solid solution $\text{Sr}_{1.9}\text{La}_{0.1}\text{Nb}_2\text{O}_7$

Hiram Joazet Ojeda-Galván^{1,2}  | Ma. del Carmen Rodríguez-Aranda¹  |
Ángel Gabriel Rodríguez¹  | Javier Alanis^{1,3}  | Jorge Íñiguez^{5,6}  |
María Eugenia Mendoza⁴  | Hugo Ricardo Navarro-Contreras¹ 

¹Coordination for the Innovation and Application of Science and Technology (CIACYT), Autonomous University of San Luis Potosí, San Luis Potosí, 78000, Mexico

²Center for Research in Health Sciences and Biomedicine (CICSAB), Autonomous University of San Luis Potosí, San Luis Potosí, 78000, Mexico

³Science Faculty, Autonomous University of San Luis Potosí, San Luis Potosí, 78000, Mexico

⁴Institute of Physics, Luis Rivera Terrazas, Meritorious Autonomous University of Puebla, Puebla, 72570, Mexico

⁵Materials Research and Technology Department, Luxembourg Institute of Science and Technology (LIST), Esch-sur-Alzette, L-4362, Luxembourg

⁶Physics and Materials Research Unit, University of Luxembourg, Belvaux, L-4422, Luxembourg

Correspondence

Javier Alanis and Hugo R. Navarro-Contreras, Coordination for the Innovation and Application of Science and Technology (CIACYT), Autonomous University of San Luis Potosí, Álvaro Obregón 64, San Luis Potosí, S.L.P. 78000, Mexico.
Email: javier.alanis.perez@hotmail.com; hnavarro@uaslp.mx

Funding information

Consejo Nacional de Ciencia y Tecnología, Grant/Award Numbers: Ciencia Básica 256788, Estancias Posdoctorales 2018(1), Problemas Nacionales 2015-01-986; Secretaría de Educación Pública: Estancias Posdoctorales PRODEP 2019; Fonds National de la Recherche Luxembourg, Grant/Award Number: FNR/P12/4853155

Abstract

Ceramic powder samples of the perovskite-slab-layered polycrystalline $\text{Sr}_{1.9}\text{La}_{0.1}\text{Nb}_2\text{O}_7$ (SLNO1) thermoelectric solid solution were prepared via solid-state reaction. The Raman effect was studied as a function of temperature between 27°C and 400°C (at ambient pressure) and pressures up to 11.6 GPa (at room temperature). The atomic disorder introduced by the La atoms produced phonon lines that were broader than those of $\text{Sr}_2\text{Nb}_2\text{O}_7$ (SNO). We detected a temperature-induced phase transition at $T_{i-c} = 247 \pm 5^\circ\text{C}$ (ambient pressure) and a pressure-induced phase transition at $P_{i-c} = 6.74 \pm 0.25$ GPa (room temperature), which correspond to the reported SNO incommensurate-to-commensurate phase transitions at 215°C (atmospheric pressure) and $P_{i-c} = 6.54 \pm 0.25$ GPa (27°C), respectively. In this paper, the phenomenological and structural differences between SNO and SLNO1 are discussed based on density functional theory calculations of $\text{Sr}_{2-x}\text{La}_x\text{Nb}_2\text{O}_7$ ($x = 0.0625$ and 0.125) supercells.

KEYWORDS

DFT, Grüneisen parameters, high pressure, layered perovskite, phase transition

1 | INTRODUCTION

The Brandon–Megaw-layered perovskite family of materials with the general formula $A_nB_nX_{3n+2}$ (where n indicates the number of BX_6 octahedra per layer) is of great interest because of its ferroelectric, thermoelectric (TE), and photocatalytic properties.^[1–4] In particular, some members of this family are promising TE materials. One example is the $n = 4$ strontium niobate $Sr_2Nb_2O_7$ (SNO), which offers a particularly low total thermal conductivity (κ) and large Seebeck coefficient (S).^[5] However, its electrical conductivity (σ) is inadequate given its insulating character,^[5] which limits its figure of merit $ZT = TS^2\sigma/\kappa$. Hence, several efforts have been made to improve the conductivity of SNO via the substitution of Sr^{2+} by La^{3+} to form $Sr_{2-x}La_xNb_2O_7$ (SLNOx).^[5–7] The additional charge provided by the La ions results in quasi-one-dimensional metallic behavior in the a -axis direction, compared to the b - and c -axis directions, ($\sigma_a \gg \sigma_c > \sigma_b$).^[8] Similar behavior is exhibited by the thermal conductivity ($\kappa_a \gg \kappa_c > \kappa_b$).^[6] These high electric and thermal conductivity anisotropies are observed for all members of the Brandon–Megaw family with electronic free charges.^[8–10]

To further analyze the TE properties of SLNOx, κ can be divided into the sum of electronic (κ^e), phononic acoustic (κ^{Ac}), and phononic optical (κ^{Op}) parts such that $\kappa = \kappa^e + \kappa^{Ac} + \kappa^{Op}$. From the reported phenomenon that σ increases and κ decreases as x (the La fraction) increases in SLNOx,^[5] we can infer that the κ^e contribution to κ is minor when compared with the dominant phononic contributions. In addition, as the acoustic velocities in SLNOx ($x = 0$) ($v_a \sim v_b \sim v_c$)^[3] do not reflect the high anisotropy reported for κ , we can infer that κ^{Op} is the dominant contributor to κ . This unusual behavior ($\kappa^{Op} > \kappa^{Ac}$) has been previously reported in the layered hexagonal $Ge_2Sb_2Te_5$ phase.^[11]

Given these considerations, research on SLNOx optical modes is of great importance. In this work, we report on the preparation, structure, Raman spectroscopic characterization, and theoretical calculation of strontium niobate lanthanum-doped $Sr_{1.9}La_{0.1}Nb_2O_7$.

2 | EXPERIMENTAL AND COMPUTATIONAL METHODS

2.1 | Experimental methods

The SLNO1 solid solution was prepared via the solid-state reaction of stoichiometric quantities of the oxides La_2O_3 (Sigma Aldrich, 99.999%), SrO (Sigma Aldrich, 99.999%), and Nb_2O_5 (Sigma Aldrich, 99.99%). The oxides were

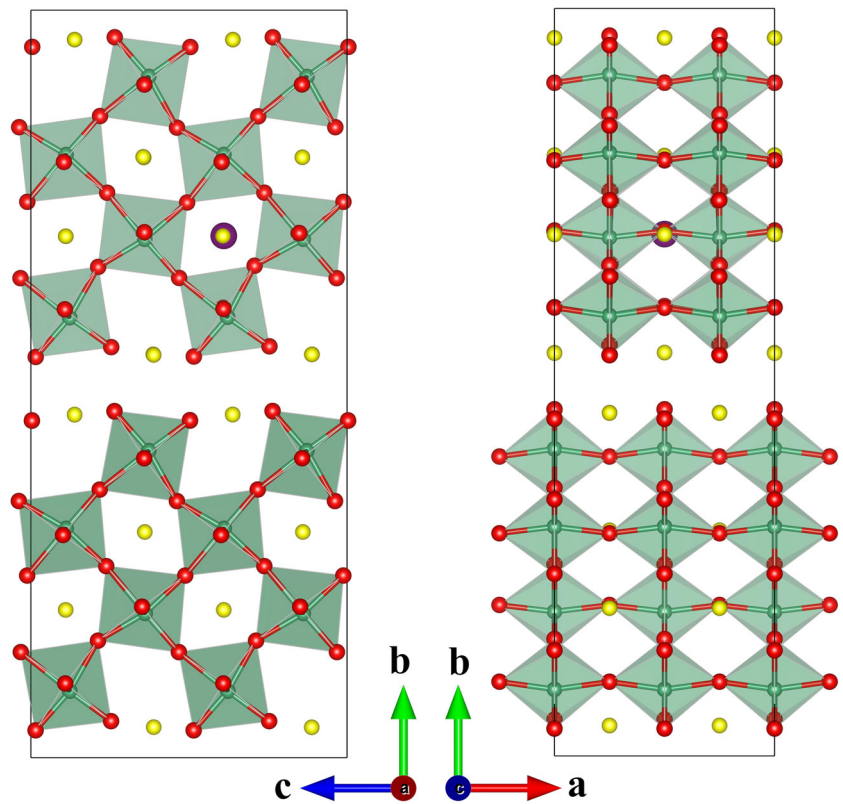
mechanically mixed and heated at 1450°C for 7 h. The calcined powders were reground and uniaxially pressed into pellet form at 28.5 MPa. These pellets were subsequently sintered at 1400°C for 2 h. The crystal structure of the sample was characterized via X-ray diffraction (XRD; PANalytical Empyrean, $\lambda = 1.54 \text{ \AA}$, X'Celerator detector). The surface morphologies of the pellets were observed by scanning electron microscopy (JSM 5400LV JEOL).

Raman scattering measurements were performed using a Jobin-Yvon T64000 spectrometer in triple configuration. A multichannel charge-coupled device (CCD) cooled to 140 K using liquid nitrogen served as the detector. The sample was analyzed in backscattering geometry $z(xy)z$, using the 532-nm line of a solid-state laser. The temperature of a small chip from the compressed pellet sample was controlled using an environmentally protected chamber. The chamber was equipped with an optically transparent window, heating system, and N_2 pressure (1 atm). The sample was placed inside a 6-mm-deep ceramic cup so that it was heated from all sides except above. The sample was allowed to thermally stabilize for 10 min to the preset temperature. Using a CCD as a photodetector and a grating with 1,800 grooves/mm, the spectral resolution was $0.6 \text{ cm}^{-1}/\text{pixel}$. The sample was allowed 10 min to stabilize thermally to the preset temperature. Given the compressed granular fused morphology of the sample, no particular selection rule considerations applied. Raman measurements were performed at various pressures that were recorded using a second spectrometer (HORIBA XploRA PLUS micro-Raman spectrometer) with a diamond anvil cell (Diacell CryoDAC-Mega). Additional experimental details may be found in Alanis et al.^[2]

2.2 | Simulated systems

Structurally, the parent compound strontium niobate $Sr_2Nb_2O_7$ (SNO) adopts the space group $Cmc2_1$ with an incommensurate (IC) part, mainly due to the displacement of interlaminar Sr atoms in the bc plane at ambient temperature and pressure. The IC part vanishes at 215°C.^[1] To perform density functional theory (DFT) calculations, we used the reported $Cmc2_1$ $Sr_2Nb_2O_7$ structure^[12] to construct supercells in which some Sr ions were replaced with La ions. These supercells represented the $Sr_{2-x}La_xNb_2O_7$ solid solutions with $x = 0.0625$ and $x = 0.125$ (Figure 1). The supercell size ($a' = 2a$ and $c' = 2c$) was selected as the minimum cell size to avoid unlikely La ion ordering (i.e., a string of La ions on the a - or c -axis). Given this supercell containing 32 Sr ions with only two different crystallographic

FIGURE 1 An illustration of a $Cmc2_1$ orthorhombic $Sr_{2-x}La_xNb_2O_7$ ($x = 0.0625$) supercell structure. The purple, yellow, green, and red balls represent La, Sr, Nb, and O ions, respectively. The shaded polyhedra are O_6 groups



positions and a homogeneous distribution of La ions (one La ion substitution per perovskite layer), we obtained two different structures corresponding to the substitution of one La ion per supercell and nine structures corresponding to the substitution of two La ions per supercell.

2.3 | First principle methods

First principle calculations were performed using DFT as implemented in the Vienna Ab Initio Simulation Package (VASP).^[13] The generalized gradient approximation (GGA) was used with the Perdew–Burke–Ernzerhof for Solids (PBEsol) scheme^[14] to describe the exchange and correlation potentials. We used Projector-Augmented Wave (PAW)^[15] pseudopotentials that were used to represent the ionic cores. We explicitly solved for the following electrons: Sr's 4s, 4p, and 5s ($10e^-$); La's 5s, 5p, 5d, and 6s ($11e^-$); Nb's 4s, 4p, 4d, and 5s ($13e^-$); and O's 2s and 2p ($6e^-$). The plane wave expansion energy cutoff was 500 eV, and a $3 \times 1 \times 3$ Monkhorst–Pack^[16] k -point grid was implemented. The effects of external hydrostatic pressures of up to 20 GPa were included in the trace of the stress tensor as implemented in VASP, to obtain the bulk modulus coefficients for the studied material. All of our calculations were performed using the 176-atom $Sr_{2-x}La_xNb_2O_7$ supercells described in the previous section.

3 | RESULTS

3.1 | Crystal structure and microstructure

The sample microstructure is dominated by plate-like crystallites (Figure S1a), in which the surface normal vector of each flake is parallel to the direction of the b -axis, much like in SNO.^[1] The grains or melted nodules exhibit a diversity of convoluted shapes that appear segmented and typically include 30–50 stacked terraces. The height of a typical terrace is $\sim 0.25 \mu\text{m}$ (Figure S1b). A representative medium-sized nodule has dimensions of $25 \mu\text{m} \times 40 \mu\text{m} \times 15 \mu\text{m}$. These nodules vary in a continuous distribution of sizes, but the predominant nodule volume is approximately $15,000 \mu\text{m}^3$. Many grains appear melted and form a semicontinuous, connected platform. In many instances, the flakes intersect with each other at slightly deviated orientations relative to the normal of the $\{080\}$ planes. Techniques for estimating grain sizes such as applying the Scherrer equation to the XRD linewidth assume specific forms and dimensions that are not suitable for analysis of these crystallite structures.

The XRD pattern of the sample is shown in Figure S1c. The peak positions of the SLNO1 sample match well with the SNO space group $Cmc2_1$, as reported by the International Centre for Diffraction Data (PDF 05-001-0348), and no secondary phases are found. Compared with the spectra of similar SNO samples,^[1] the

largest increases in peak intensity for the SLNO1 sample are observed for the planes that contain the A ion crystallographic position (i.e., planes containing Sr and La ions).

Structural refinement was performed using the Rietveld method; the refined cell parameters and atomic positions are summarized in Table S1. An agreement index R_{wp} of 8.4 was achieved (goodness of fit = 3.18). The refinement indicates a degree of preferred orientation ($\eta = 9.5\%$, March–Dollase)^[17] toward the (080) planes and a preference for La ion occupation of the interlaminar A positions. The refined cell parameters are shown in Table S2. An approximately 0.15% contraction in cell parameter b occurs due to ionic substitution, and the calculations indicate simultaneous increases of 0.12% and 0.11% in the lengths of the a - and c -axes in SLNO1, respectively. However, it should be noted that the changes in dimensions are -0.04 Å for b and only 0.004 Å for a and -0.007 Å for c . Additionally, the introduction of La causes a complicated distortion of the A-site cations along with the rotational modulation of oxygen octahedra.

3.2 | $\text{Sr}_{2-x}\text{La}_x\text{Nb}_2\text{O}_7$ ($x = 0.0625$ and 0.125) supercell calculations

3.2.1 | Structure

The calculations indicate a decrease in volume with increasing La ion content in $\text{Sr}_{2-x}\text{La}_x\text{Nb}_2\text{O}_7$ ($x = 0.0625$

and 0.125) supercells (Table S3). The structures with La ion interlaminar occupation exhibit the lowest energies and largest reductions in the cell parameter b (Table S3). These results are consistent with our experimental observations of the preferential occupation of La ions at interlaminar A positions and contraction of the cell parameter b .

3.2.2 | Bulk modulus calculations

We investigated the systems with the lowest energies (the interlaminar structures) for each composition x at pressures up to 20 GPa (Figure 2). The bulk modulus coefficients determined using the Murnaghan linear expansion^[18,19] and the ratios of relative compressibility along the a , b , and c crystallographic axes for the lowest energy structures for each value of x are summarized in Table 1. The V_0 value is fixed to the initial $P = 0$ value in each composition. As the La content increases, the bulk modulus increases, while the relative compressibility decreases.

3.2.3 | Electronic DOS

We analyzed the electronic density of states (DOS) and its projection (pDOS) for the $\text{Sr}_{2-x}\text{La}_x\text{Nb}_2\text{O}_7$ ($x = 0.0625$ and 0.125) structures. The overall band structure of the

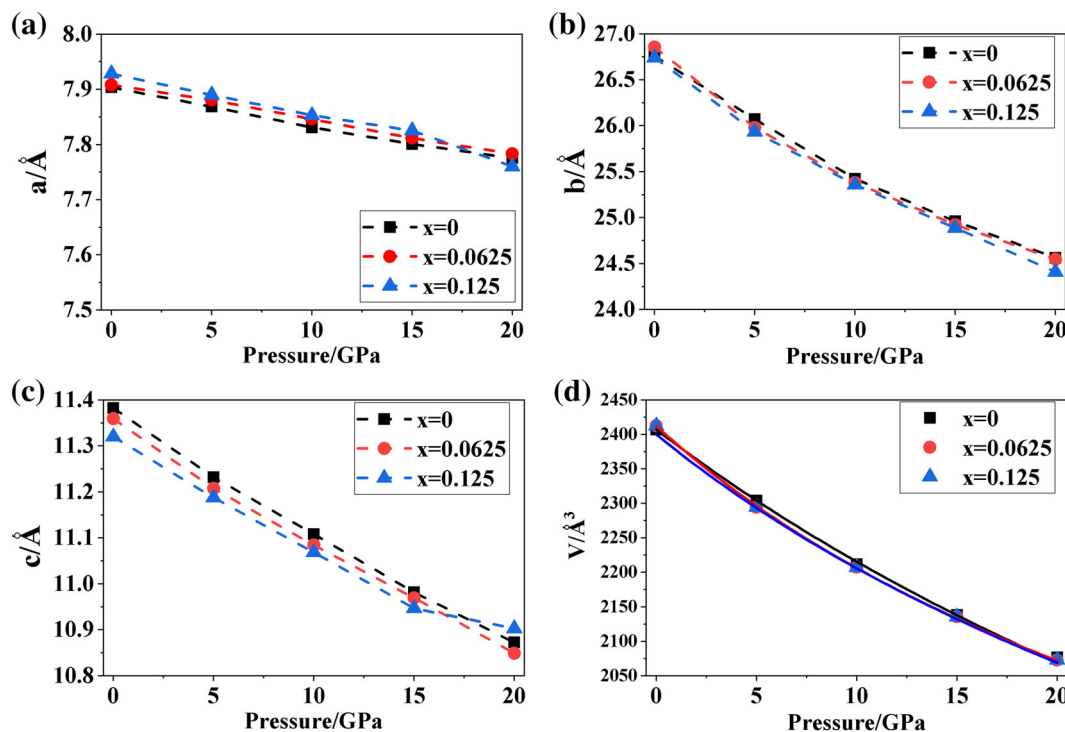


FIGURE 2 Calculated $\text{Sr}_{2-x}\text{La}_x\text{Nb}_2\text{O}_7$ ($x = 0.0625$ and 0.125) cell parameters at $T = 0$ K. The solid lines represent Murnaghan equation of state fits for each phase. Reported values (theoretical) for $\text{Sr}_2\text{Nb}_2\text{O}_7$ are shown for comparison

TABLE 1 Calculated bulk modulus coefficients B_0 and B_1 and ratios of relative lattice deformations along the a , b , and c crystallographic axes for the $\text{Sr}_{2-x}\text{La}_x\text{Nb}_2\text{O}_7$ ($x = 0, 0.0625$, and 0.125) solid solutions

$\text{Sr}_{2-x}\text{La}_x\text{Nb}_2\text{O}_7$	B_0 (GPa)	B_1	$(\Delta a/a_0)/(\Delta a/a_0): (\Delta b/b_0)/(\Delta a/a_0): (\Delta c/c_0)/(\Delta a/a_0)$
0	100(8)	3.9(9)	1: ~5.5: ~3
0.0625	90(16)	4.7(23)	1: ~6.9: ~3.2
0.1	96(16)	4.1(23)	1: ~5.8: ~2.6
0.125	100(17)	3.7(23)	1: ~5.3: ~2.3

Note: Extrapolated values for $x = 0.1$ and reported values for $x = 0$ ^[2] are shown.

DOS in Figure 3a is analogous to that reported for the $n = 5$ and La-doped $n = 4,5$ $\text{Sr}_n\text{Nb}_n\text{O}_{3n+2}$ Brandon–Megaw structures,^[20–22] as well as for the $\text{Sr}_2\text{Nb}_2\text{O}_7$.^[23] The additional charge provided by the substituted La ion is distributed into the NbO_6 perovskites at both compositions.

For further theoretical analysis, we analyzed the pDOSs of the Nb ions; the pDOSs of the Nb d orbitals are shown in Figure 3b. The energy difference between these d orbitals is related to the electronic conduction anisotropy (the reported σ ratios along the a , b , and c crystallographic axes are ~200:1:10 for both $x = 0.2$ and 0.4),^[9,10,24] where the bottom of the conduction band is taken mainly from the d_{xy} and d_{xz} orbitals (a -axis-related orbitals). The position of La (interlaminar, intralaminar, or inter/intralaminar) does not significantly affect the DOS or pDOS.

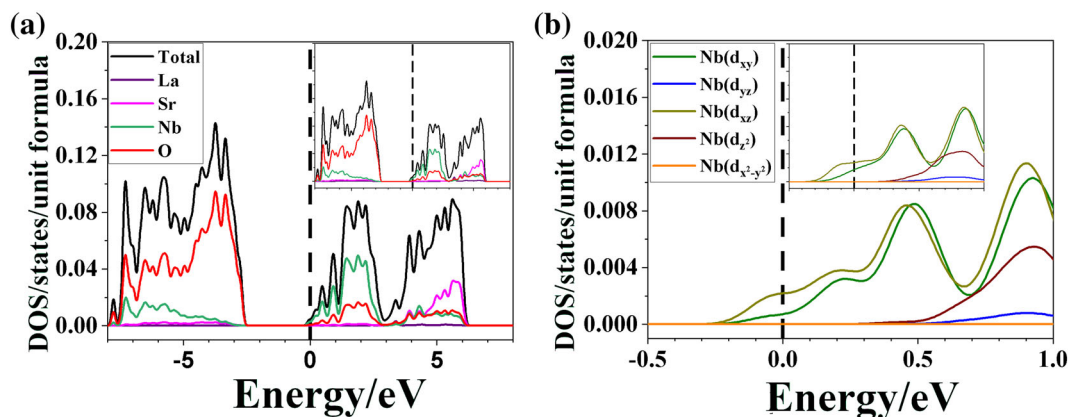
The variation in the Nb d orbitals with external hydrostatic pressure is shown in Figure S2. A small increase in the electronic density is observed at the bottom below the Fermi level for the d_{xy} and d_{xz} orbitals. Thus, the electrical conductivity along the a -axis (σ_a) is expected to increase with pressure, as has been reported in other perovskites.^[25] While the other d orbitals (related to σ_b and σ_c) undergo small changes, the high σ

anisotropy of the material is expected to persist because the aforementioned orbitals do not reach the Fermi level.

Figure S3 shows the pDOSs of intralaminar and interlaminar Nb ions. The electronic density at the intralaminar Nb ions shows a greater increase than that at the interlaminar Nb ions. The additional charge causes the distorted NbO_6 octahedra in $\text{Sr}_{2-x}\text{La}_x\text{Nb}_2\text{O}_7$ ($x = 0.0625$ and 0.125) to be less misaligned than in SNO. These structural changes explain the decreased cell parameters and volumes mentioned in Sections 3.1 and 3.2.1. In addition, the external hydrostatic pressure-mediated structural behavior mentioned in Section 3.2.2 can be driven by the larger La ion radius and the less distorted misaligned NbO_6 octahedra (because of the additional charge provided); the La ions increase the resistance to compression, and the less misoriented octahedra improve cell compression.

3.3 | Temperature-dependent Raman spectra

The Raman spectra of the SLNO1 solid solution measured at 27°C, 107°C, 207°C, 307°C, and 400°C are shown in Figure 4. The plots are separated into two spectral

**FIGURE 3** (a) DOS and pDOS in each atom for $\text{Sr}_{2-x}\text{La}_x\text{Nb}_2\text{O}_7$ ($x = 0.0625$) and (b) pDOS in Nb atoms d orbitals for $\text{Sr}_{2-x}\text{La}_x\text{Nb}_2\text{O}_7$ ($x = 0.0625$). Insets are the respective graphics for $x = 0.125$ and dashed lines indicates the Fermi level

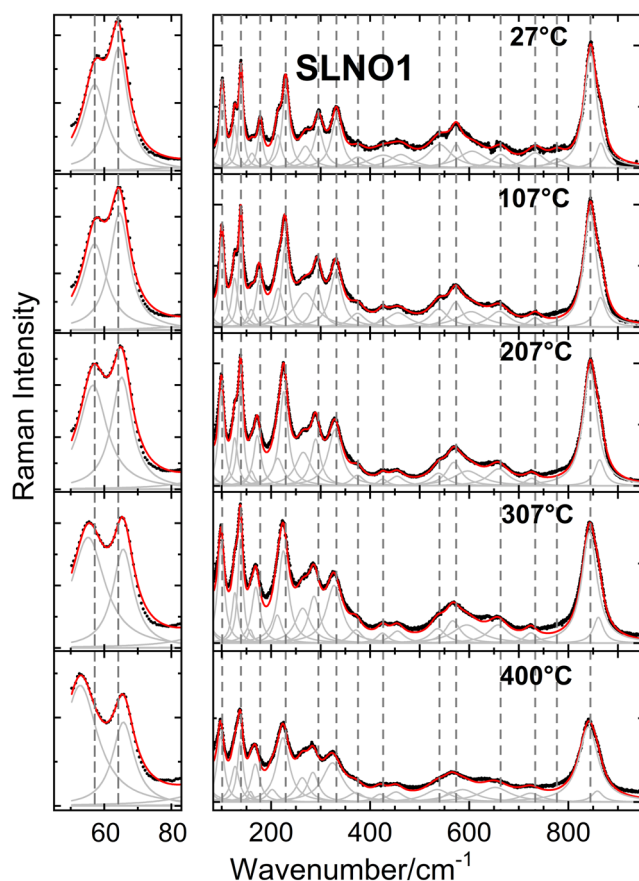


FIGURE 4 Raman spectra of the perovskite layered solid solution SLNO1, from room temperature to 400°C. Both spectral regions differ by a factor of two on the vertical scale. That is, the actual relative intensities of the data in the first regions are equivalent to those in the second frames multiplied by a factor of 0.5. The continuous red lines represent the fit produced by 23 phonons. The dashed lines are drawn as a visual aid. The Lorentzian fitting bands are shown in gray

regions. The first region from 50 to 80 cm^{-1} can effectively visualize the specific responses of the two phonon bands in the region. It also demonstrates the wavenumber hardening of the phonon band centered at $\sim 55 \text{ cm}^{-1}$ (room temperature and zero applied pressure), which is associated with the ferroelectric–paraelectric transition as the temperature increases. The phonon responses between 80 and 1,000 cm^{-1} are also shown. The spectral range that could be reliably examined begins at 50 cm^{-1} because strong Rayleigh scattering produced by the granular consistency of the samples prevented us from resolving phonons below this wavenumber. In Figure 4, the dashed lines indicate 16 of the directly visible phonon lines. The red line shows the result of a Lorentzian function fit that indicates the presence of 23 total phonons. During fitting, care was exercised to consider information from the literature regarding the presence of phonons. The infrared and Raman spectra in

the literature are consistent with our spectra, particularly in the low-frequency region.^[1,26–29] The phonons are labeled according to their correspondence to those of the parent compound SNO in Ref. [1].

Factor group analysis using the Spectral Active Modes program from the Bilbao crystallographic server was used to predict the number of phonons.^[30] Crystallographic information from PDF 05-001-0348 about the (*Cmc*2₁ space group and all atoms located at Wickoff site 4a) was used as input to the program. The resulting predicted phonon counts are 21 *A*₁, 11 *A*₂, 10 *B*₁, and 21 *B*₂ (acoustic modes not included), which represent 63 Raman-active modes.

The SLNO1 phonon positions and their relative intensities at both 27°C and 400°C are summarized in Table 2. The observed phonon positions and relative intensities in SNO^[1] are included for comparison. Overall, 17 of the equivalent phonons appear to exhibit the same relative intensities, whereas five exhibit diminished relative intensities. Among the 23 observed phonons in SLNO1, only *f*1 appears to exhibit a larger intensity in SLNO1 than in SNO. This exercise confirms that the assignments of most of the observed phonons in SLNO1 versus the Sr₂Nb₂O₇ parent compound are correct with two possible exceptions: the phonons labeled *f*8 and *f*33 in SLNO1, which have weak intensity and are shifted by 13 and 16 cm^{-1} with respect to the equally enumerated phonons in SNO.

The introduction of heavier La atoms at the Sr sites inside the Sr₂Nb₂O₇ lattice without any special ordering is expected to affect the frequencies of all the aforementioned phonons. The La atoms serve to broaden the phonon frequencies and affect the relevant wavenumbers simply because of the mass difference. Indeed, this is the case for the majority (21/23) of the phonons observed at 27°C. Two phonons are observed at almost identical wavenumbers, and 14 out of the 23 phonons are blueshifted. Among the rest, seven appear slightly shifted toward lower wavenumbers. As is discussed in the next section, because the wavenumber slope tends to decrease substantially as the temperature increases in SLNO1, 14 phonons are blueshifted in SLNO1 at 400°C, whereas only six are blueshifted in SNO. Similarly, an experimental study indicated that at room temperature, 22 of the 23 phonons observed are systematically broader in SLNO1 than in SNO; the lower frequency phonons exhibit the largest broadenings, as in many Nb-based perovskites.^[31] Almost all differences in the full width at half maximum (FWHM) are in the range of 2–20 cm^{-1} . As the temperature increases, the FWHM increases for most phonons except *f*35.

Figure 5 plots some illustrative phonon positions derived from the SLNO1 spectra as a function of

TABLE 2 Summary of the observed phonon positions at 27°C and 400°C, phonon interpolation $\omega_i(T = 0 \text{ K}) = \omega_{i,0}$ in cm^{-1} (interpolated values), wavenumber–temperature slopes $(\frac{\partial \omega_i}{\partial T})_P = m_T$ in cm^{-1}/K and Grüneisen temperature parameters $\gamma_{i,T}$ in $\text{Sr}_{1.9}\text{La}_{0.1}\text{Nb}_2\text{O}_7$ (SLNO1)

Phonon name	$T = 27^\circ\text{C}$		$T = 400^\circ\text{C}$				SLNO1			
	SNO ^[1]	SLNO1	SNO ^[1]	SLNO1	SNO ^[1]	SLNO1	$T < 247^\circ\text{C}$		$T > 247^\circ\text{C}$	
	ω_i	ω_i	ω_i	ω_i	Intensity	Intensity	m_T	$\gamma_{i,T}$	m_T	$\gamma_{i,T}$
<i>f1</i>	55.6	57.11	54.9	52.78	M	S	−0.005	2.479	−0.023	11.260
<i>f3</i>	64.4	64.17	66.4	65.66	VS	S	0.005	−2.510	0.002	−0.688
<i>f6</i>	102.5	101.20	99.1	97.55	S	S	−0.010	2.722	−0.010	2.722
<i>f8</i>	125.5	126.02	127.3	127.09	S	M	0.001	−0.260	0.001	−0.260
<i>f9</i>	138.6	138.93	137.7	137.61	S	S	−0.004	0.910	−0.004	0.910
<i>f11</i>	161.2	161.09	158.4	158.47	W	VW	−0.010	1.770	−0.010	1.770
<i>f12</i>	177.4	177.88	167.5	167.86	M	M	−0.029	4.669	−0.029	4.669
<i>f15</i>	212.9	213.23	216.6	201.93	M	M SH	−0.004	0.570	−0.108	11.693
<i>f16</i>	228.3	229.25	224.0	223.51	VS	S	−0.021	2.606	−0.011	1.414
<i>f17</i>	264.6	269.05	265.7	262.58	W-SH	W	−0.018	1.975	−0.018	1.975
<i>f19</i>	296.2	295.38	288.0	284.06	M	M	−0.032	3.106	−0.032	3.106
<i>f21</i>	335.1	331.71	328.4	323.76	M	M	−0.018	1.610	−0.018	1.610
<i>f23</i>	378.3	375.31	373.9	371.18	W	W	−0.006	0.435	−0.006	0.435
<i>f24</i>	427.5	426.16	424.2	419.94	W	W	0.002	−0.112	−0.030	1.997
<i>f25</i>	456.0	461.75	454.5	452.05	W	VW	−0.017	1.081	−0.017	1.081
<i>f26</i>	536.9	540.00	533.7	535.44	W	W	−0.005	0.280	−0.005	0.280
<i>f27</i>	570.1	573.62	562.7	564.14	M	M	−0.026	1.342	−0.026	1.342
<i>f28</i>	589.0	605.71	586.4	586.48	W-SH	W SH	−0.045	2.132	−0.045	2.132
<i>f30</i>	664.1	663.31	655.0	652.10	W	W	−0.026	1.125	−0.026	1.125
<i>f32</i>	731.1	733.20	719.0	723.68	W	W	−0.021	0.858	−0.021	0.858
<i>f33</i>	790.7	776.98	787.7	774.21	W	VW	−0.069	2.578	Disappears at 67°C	
<i>f34</i>	845.8	844.54	845.4	840.47	VS	VS	−0.005	0.168	−0.018	0.621
<i>f35</i>	864.9	865.40	861.5	858.37	S-Sh	S	−0.016	0.529	−0.016	0.529
Volumetric thermal expansion $3.37 \times 10^{-5} \text{ K}^{-1}$										

Note: Only the phonons whose response with the temperature could be reliably followed are shown. By comparison, the corresponding phonons observed in SNO^[1] are also included, and of their qualitative intensities are also presented.

temperature. The red lines illustrate linear fits to the temperature responses of most phonons. The temperature slopes of all phonons observed are summarized in Table 2. Although the observed phonons exhibit specific responses, softening is observed with increasing temperature for a majority of the phonons shown. Only four phonons exhibit hardening responses. The following important considerations are discussed in subsequent sections because several phonons exhibit nonlinear responses, slope discontinuities, or both:

I. Whereas 20 phonons exhibit softening responses, the remaining three (*f3*, *f8*, and *f24*) exhibit hardening as the temperature increases in SLNO1. Similar responses are observed for the corresponding phonons

f3 and *f8* in $\text{Sr}_2\text{Nb}_2\text{O}_7$. In contrast, *f24* exhibits monotonic softening with increasing temperature.

II. Six phonons (*f1*, *f3*, *f15*, *f16*, *f24*, and *f34*) exhibit a change in temperature slope above 247°C (i.e., no phonons display a change in temperature response in SLNO1 at the well-known phase transition at 215°C of the parent compound SNO).

As is well known in Raman spectroscopy^[32] and reported by Kojima et al. ($\text{Sr}_2\text{Nb}_{2-x}\text{Ta}_x\text{O}_7$)^[33] and Shabbir et al. ($\text{Sr}_{2-x}\text{Ba}_x\text{Nb}_2\text{O}_7$)^[34] for longitudinal acoustic phonons in the vicinity of the IC transition temperature T_{i-c} , second-order phase transitions may reflect a change in the temperature wavenumber coefficient of some Raman bands or the gradual but final disappearance of some

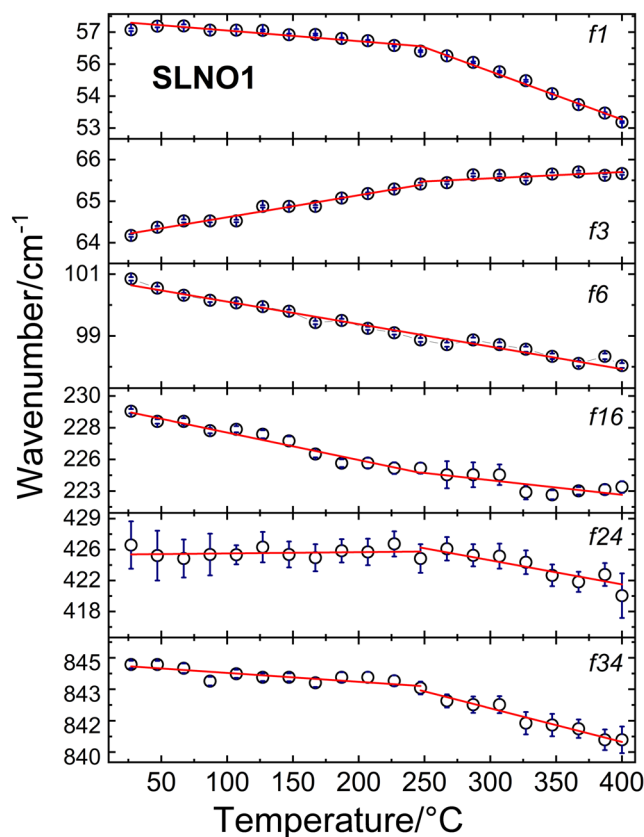


FIGURE 5 Plot of the observed phonon band positions for the perovskite-layered solid solution SLNO1. For some phonons, the experimental position uncertainty (indicated with error bars for all of the other phonons) is encompassed by the symbol size

Raman bands at the phase transition critical temperature. This originates from a Raman-active order parameter, collective excitation in the transforming structure, or phonon lines that are either permitted or forbidden in the new crystalline structure adopted by the compound after the transition. Therefore, the measured Raman spectra of SLNO1 at different temperatures provide evidence of a transition from the IC phase to the $Cmc2_1$ phase in the solid solution at $247^\circ\text{C} \pm 5^\circ\text{C}$. The order parameter in SLNO1 conducive to the transition at 247°C in analogy to SNO must be the dipolar electric moment present in the phase adopted at room temperature.

It is important to note that the IC phase is preserved via the substitution of ions, possibly due to the laminar structure. Examples of this include the substitution of Ba ions for Sr ions to form $\text{Sr}_{2-x}\text{Ba}_x\text{Nb}_2\text{O}_7$ ($x \leq 0.32$).^[34] Ion substitution decreases T_{i-c} , possibly due to the larger ionic radius of Ba compared to Sr. In SLNO1, the increased T_{i-c} may be caused by the less distorted misaligned NbO_6 octahedra (generated by the additional charge provided).

3.4 | Detailed comparison of the temperature slopes of SLNO1 and SNO

Based on a detailed comparison of the temperature responses of the SLNO1 and SNO phonons, the following conclusions can be drawn:

- I. The SLNO1 phonon temperature slopes tend to be more negative than those of SNO. As mentioned earlier, 20 phonons exhibit negative responses in SLNO1, whereas only 14 exhibit negative responses in SNO.
- II. The additional phonons that exhibit negative responses in SLNO1 are f_1 , f_{15} , f_{17} , f_{25} , f_{26} , and f_{34} .
- III. The following phonons exhibit larger negative responses in SLNO1 than in SNO: f_9 , f_{11} , f_{12} , f_{27} , f_{28} , f_{33} , and f_{35} .
- IV. Only phonon f_8 exhibits a weak positive slope in SLNO1, but a negative one in SNO.
- V. Only phonon f_{24} exhibits a larger positive slope in SLNO1 than in SNO.

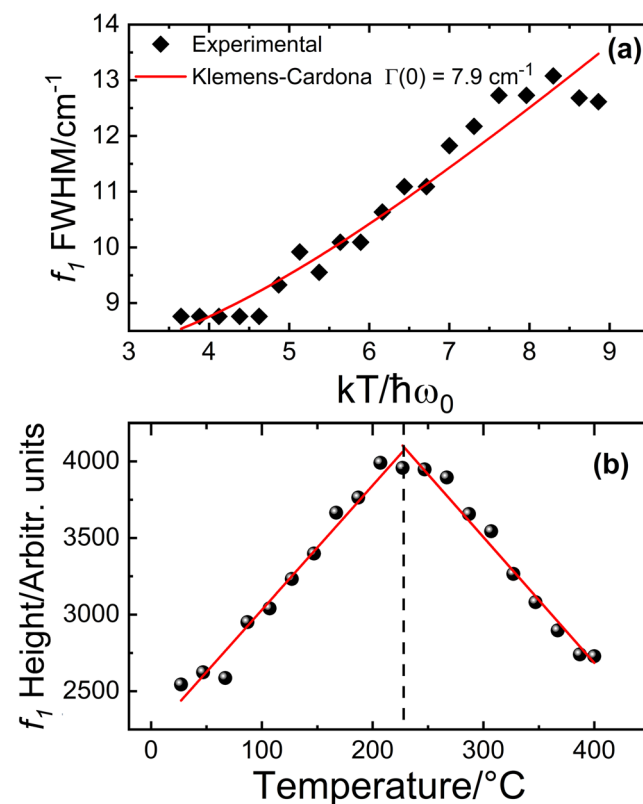


FIGURE 6 Plot of the (a) full width at half maximum of the f_1 phonon of SLNO1. The red line is the Klemens-Cardona model fit and (b) temperature dependence of the intensity of the f_1 phonon mode

3.5 | FWHM values and intensity dependence of the soft phonon $f1$

Figure 6a plots the line-shape broadenings (FWHM values) of phonon $f1$ in SLNO1. This phonon is associated with the order parameter responsible for the ferroelectric–paraelectric transition at high temperature, as observed in SNO.^[1] The phonon presents uniform softening as the temperature increases; however, an interesting inflexion in its intensity is observed at temperatures above 210–260°C (i.e., around the transition observed at 247°C \pm 5°C in Figure 6b). The intensity increases monotonically up to this temperature and then decreases steadily at higher temperatures. This provides additional evidence of the structural transformation between the IC and commensurate ferroelectric phases in $\text{Sr}_{1.9}\text{La}_{0.1}\text{Nb}_2\text{O}_7$ at this temperature.

As discussed by Alanis et al.,^[1] we used the theoretical analysis of Klemens and Cardona^[35,36] and the so-called symmetrical three-phonon coupling approximation to fit the observed FWHM of the phonon $f1$ as a function of temperature (Figure 6a). The red line indicates the fit obtained using the Klemens–Cardona decay model:

$$\Gamma(T) = \Gamma(0)[1 + n(\omega_1, q) + n(\omega_2, -q)], \quad (1)$$

where $n(\omega, q) = \left[e^{\frac{\hbar\omega}{k_B T}} - 1 \right]^{-1}$ is the Bose–Einstein phonon population factor and $\Gamma(0)$ is a fitting parameter. In the Klemens–Cardona model, $\omega_{1,2} = \Omega/2$, where Ω is the extrapolated zero-temperature phonon frequency assuming that the optical Raman phonon decays as two acoustical phonons of opposite q that belong to the same branch. Hence, in this case, $n(\omega_1, q) = n(\omega_2, -q) = \left[e^{\frac{\hbar\Omega}{2k_B T}} - 1 \right]^{-1}$. In Figure 6a, the Klemens–Cardona model provides a satisfactory fit at most temperatures and provides a value of $\Gamma(0) = 7.9 \text{ cm}^{-1}$, for $f1$. The FWHM at a temperature of zero is substantially broader than that calculated for SNO ($\Gamma(0) = 0.84 \text{ cm}^{-1}$).^[1] The difference is almost one order of magnitude, as expected from the random distribution of La atoms at the A sites (with a preference for La ions occupying the interlaminar A sites). This produces disorder-induced broadening that is comparable with that observed in the layered perovskite compound $\text{Bi}_5\text{FeTi}_3\text{O}_{15}$ ($\Gamma(0) = 8.7 \text{ cm}^{-1}$).^[37]

3.6 | Pressure-dependent Raman spectra

Figure 7 shows the Raman spectra measured for the SLNO1 solid solution at various pressures. Two of the

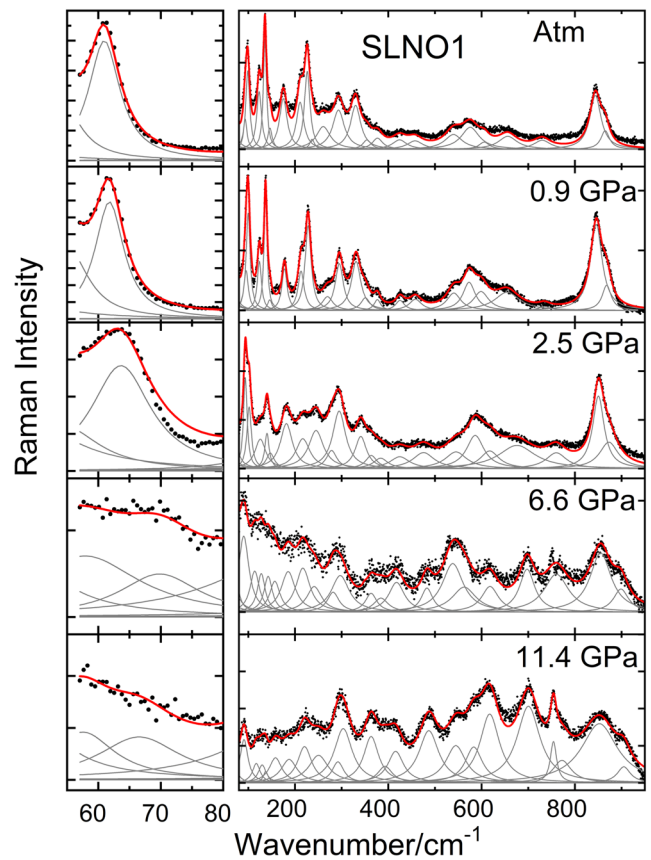


FIGURE 7 Raman spectra of the perovskite layered solid solution SLNO1 inside the diamond cell and under hydrostatic pressures from zero to 11.4 GPa

pressures considered are below the transition pressure (Figure 8), one is near the transition pressure at ~ 6.6 GPa, and another one is above it at 11.4 GPa (the maximum applied pressure). Figure 7 also shows the Raman spectrum of the solid solution mounted in the diamond cell at atmospheric pressure.

As before, the plots in Figure 7 are separated into two spectral regions for the purpose described in Section 3.2. Again, the red line illustrates the result of the Lorentzian function fit that is used to indicate the presence of 26 phonons in total (Table S4). Several distinctive features can be noted inside the diamond cell. When the pressure is zero, several phonon bands (phonons $n1$, $f5$, $f10$, $n3$, $f20$, and $f22$) appear that do not manifest in the spectra measured in the previous temperature study, whereas phonons $f6$, $f11$, and $f21$ are no longer observed. At $P = 6.6$ GPa, a phase change occurs, and a total of 23 phonons are found. We identify this pressure-induced transition as the IC-to-commensurate $\text{Cmc}2_1$ transition of SNO reported by Alanis et al.^[12] ($P_{i-c} = 6.5 \pm 0.2$ GPa). From the

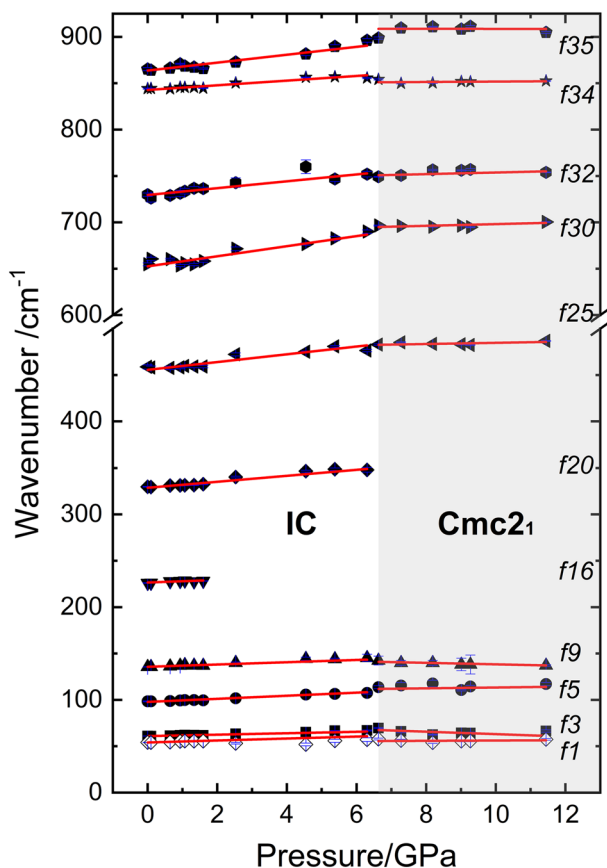


FIGURE 8 Plot of the observed phonon band positions for the perovskite layered solid solution SLNO1. For most of the phonons, the experimental position uncertainty (indicated with error bars) is encompassed by the symbol size. The critical pressure where the sample exhibits a phase transition IC \rightarrow Cmc21 is indicated by the gray shaded region

experiments, the f_{16} and f_{20} bands disappear above the critical SLNO1 pressure $P_{i-c} = 6.7 \pm 0.25$ GPa, as observed in Figure 8.

Figure 8 summarizes the peak positions of the 11 phonons whose response to the externally applied hydrostatic pressure can be observed below the critical pressure P_{i-c} and nine phonons that can be observed above this critical pressure. These phonons are summarized alongside their wavenumber pressure slopes below and above the critical pressure in Table 3.

Next, we perform a comparison analogous to that described in the wavenumber–temperature slope discussion. In particular, we compare the pressure slopes of SNO^[2] and SLNO1. Seven phonons are observed in both compounds below the critical pressure, while five phonons are observed above it. Similar to the temperature phase transition, at pressures below P_{i-c} , all seven pressure wavenumber slopes are smaller in SLNO1 than in SNO. At pressures above P_{i-c} , four out of five phonons exhibit smaller slopes in SLNO1 than in SNO. The slope of the fifth phonon, f_{25} , is larger in SLNO1 than in SNO (Table 3).

3.7 | Raman spectra after pressure removal

Figure S4 compares the Raman spectra of SLNO1 at zero pressure and after a cycle of measurements under pressure. Comparing Figures S4a and S4b shows that the spectrum changes when the sample is exposed to hydrostatic pressure. In addition, 20 phonon wavenumbers are redshifted by $0.5\text{--}3\text{ cm}^{-1}$, whereas five exhibit blueshifts

Phonon name	$P < 6.74$ GPa			$P > 6.74$ GPa		
	$\omega_{i,0}$	m_P	$\gamma_{i,P}$	$\omega_{i,0}$	m_P	$\gamma_{i,P}$
f_1	54.5	0.15	0.29	55.6	0.06	0.16
f_3	60.7	1.02	1.79	69.2	−0.49	−1.04
f_5	98.0	1.55	1.68	112.1	0.32	0.42
f_9	135.4	1.68	1.32	148.2	−1.02	−1.01
f_{16}	226.3	1.47	0.68	Disappears at ~ 6.7 GPa		
f_{20}	328.7	3.49	1.13	Disappears at ~ 2 GPa		
f_{25}	456.4	3.91	0.91	479.4	0.52	0.15
f_{30}	653.2	5.49	0.89	690.2	0.74	0.16
f_{32}	729.0	4.36	0.64	744.6	1.09	0.22
f_{34}	843.4	2.32	0.29	851.5	0.03	0.01
f_{35}	862.9	4.80	0.59	902.2	0.59	0.10
Average bulk modulus	106 GPa			133 GPa		

Note: Only the phonons whose response with the pressure could be reliably followed are shown.

TABLE 3 Summary of the observed phonons positions inside of DAC $\omega_i (P = 0 \text{ GPa}) = \omega_{i,0}$ in cm^{-1} (interpolated values), wavenumber–pressure slopes $(\frac{\partial \omega_i}{\partial P})_T = m_P$ in $\text{cm}^{-1}/\text{GPa}$ and the Grüneisen pressure parameters $\gamma_{i,P}$ for $\text{Sr}_{1.9}\text{La}_{0.1}\text{Nb}_2\text{O}_7$ (SLNO1)

of 2–12 cm^{−1}. The new phonon wavenumbers are summarized in the third column of Table S4. Phonon *f10* is no longer observable.

4 | DISCUSSION

As mentioned in Sections 3.1–3.3, the La ions preferentially occupy interlaminar A sites when they replace Sr ions in the Sr₂Nb₂O₇ structure. This type of preferential occupation has been reported for the *n* = 3 Sr₂LaTaO₁₁ Brandon–Megaw compound.^[9] Another common characteristic of these compounds appears to be the low or non-existent dependence of the *f1* phonon frequency on A site ion substitution, possibly due to the laminar compound topology. This has been reported under atmospheric pressure and room temperature conditions for *n* = 4 Brandon–Megaw compounds.^[34,38–42] We identify SLNO1 temperature and pressure phase transitions at $T = 247^\circ\text{C} \pm 5^\circ\text{C}$ and $P = 6.74 \pm 0.25$ GPa, respectively. Both transitions seem to correspond to the IC-to-commensurate *Cmc2*₁ transition. This increase in the temperature at which the first phase transition occurs ($\Delta T = 32^\circ\text{C} \pm 5^\circ\text{C}$) must result from structural changes produced by the insertion of La atoms. According to the DFT calculations, the insertion of La atoms decreases the misalignment and distortion of NbO₆ octahedra because of the additional charge provided. The DFT calculations also indicate that the IC-to-commensurate *Cmc2*₁ transition originates from the relatively “underbound” interlaminar A sites (using the same term as Daniels et al.^[12]) compared with the same binding in the intralaminar A sites. Therefore, the decrease in misalignment and distortion of NbO₆ octahedra in the IC phase further weakens the binding of the atoms in the interlaminar A sites. This situation is reflected in the delay of the IC-to-commensurate *Cmc2*₁ transition of SLNO1 compared with SNO in terms of both temperature and pressure.

Empirical analysis suggests that the increased temperature of this transition for SLNO1 could be expected. Assume a linear relationship, $T_{i-c} = a + b \times T$, about the IC-to-commensurate *Cmc2*₁ transition temperature between Sr₂Nb₂O₇ and La₂Ti₂O₇, where $a = 215^\circ\text{C}$ at $x = 0$. The slope b is 17.5 because the T_{i-c} of La₂Ti₂O₇ ($x = 2$) is 1080 K (807°C).^[43] Assuming $T_{i-c} = 247^\circ\text{C}$, this relationship gives $x = 0.108$ for the sample prepared in this paper, which is close to our experimental La composition of 0.1.

Using the dependencies of phonon frequency on temperature and pressure, we determine the Grüneisen temperature ($\gamma_{i,T}$) and pressure ($\gamma_{i,P}$) parameters for SLNO1 using the reported volumetric thermal expansion coefficient (α)^[1] and the extrapolated bulk modulus (B) calculated in

Section 3.2 and summarized in Tables 2 and 3. We calculate these parameters using the expressions in Equation 2:

$$\gamma_{i,T} = -\frac{1}{\alpha\omega_{i,0}} \left(\frac{\partial\omega_i}{\partial T} \right)_P, \gamma_{i,P} = \frac{B}{\omega_{i,0}} \left(\frac{\partial\omega_i}{\partial P} \right)_T. \quad (2)$$

The discontinuities observed in the wavenumber–temperature slopes in SNO are related to the compound’s transition to a higher symmetry paraelectric phase.^[1] In SLNO1, a similar situation holds. Likewise, that the negative wavenumber–pressure slopes tend to be larger in SLNO1 than in SNO originates from the increased resistance of the cell to compression. This occurs due to the substitution of Sr ions with La ions. This situation implies that the compressibility decreases as the La content increases; hence, the bulk modulus, which is directly proportional to the Grüneisen parameter (i.e., to the magnitude of the phonon wavenumbers temperature and pressure slopes), also increases. Finally, in the context of TE, the hydrostatic pressure does not substantially reduce the energy differences between the Nb *d* orbitals and therefore is not expected to decrease the reported σ anisotropy.

5 | CONCLUSIONS

We report a theoretical and experimental study of the structural changes induced by the substitution of La³⁺ ions for Sr²⁺ ions in the TE laminar perovskite structure Sr_{1.9}La_{0.1}Nb₂O₇. The preferential occupation of interlaminar A sites by La ions was confirmed experimentally via the Rietveld refinement of the XRD pattern of a polycrystalline sample of SLNO1 and theoretically via DFT calculations on Sr_{2-x}La_xNb₂O₇ ($x = 0.0625$ and 0.125) supercells.

In the SLNO1 sample, the coefficients that describe how 23 phonons change with temperature (at ambient pressure) and how 11 photons change with applied pressure (at room temperature) were determined experimentally. Most phonons exhibit monotonic wavenumber softening with increasing temperature, whereas the inverse behavior is observed with increasing pressure. Six phonons exhibit discontinuities in their wavenumber–temperature slopes at $T = 247^\circ\text{C} \pm 5^\circ\text{C}$ (ambient pressure). Similar discontinuities are exhibited by eight phonons at $P = 6.74$ GPa (room temperature). The two discontinuities correspond to the reported IC-to-commensurate *Cmc2*₁ temperature and pressure transitions. The Grüneisen temperature and pressure parameters for the observed phonons were calculated, and the differences observed between SNO and SLNO1 were explained based on the structural changes


predicted by DFT calculations of $\text{Sr}_{2-x}\text{La}_x\text{Nb}_2\text{O}_7$ ($x = 0.0625$ and 0.125) supercells. The La ions increase the resistance to compression and reduce the misalignment of distorted octahedra because of the additional charge provided, thereby improving the cell compressibility.

ACKNOWLEDGEMENTS

The authors acknowledge the financial support from Consejo Nacional de Ciencia y Tecnología (CONACyT) México, through the projects Problemas Nacionales 2015-01-986, Estancias Posdoctorales 2018(1), and Ciencia Básica 256788, from FAI-UASLP, CEMIESOL Project 22, and access to Laboratorio Nacional de Análisis Físicos, Químicos y Biológicos-UASLP, during the course of this research. The authors thankfully acknowledge the computer resources, technical expertise, and support provided by the Laboratorio Nacional de Supercómputo del Sureste de México, CONACYT Network of National Laboratories. J. Í. Acknowledges support from the Fonds National de la Recherche Luxembourg Fund, through grant no. FNR/P12/4853155 “COFERMAT.” J. A. acknowledges support from Secretaría de Educación Pública through Estancias Posdoctorales PRODEP 2019.

ORCID

Hiram Joazet Ojeda-Galván  <https://orcid.org/0000-0001-8521-294X>


Ma. del Carmen Rodríguez-Aranda  <https://orcid.org/0000-0003-0632-2265>

Ángel Gabriel Rodríguez  <https://orcid.org/0000-0002-0565-4236>

Javier Alanís  <https://orcid.org/0000-0001-8457-7584>

Jorge Íñiguez  <https://orcid.org/0000-0001-6435-3604>

María Eugenia Mendoza  <https://orcid.org/0000-0002-1947-7875>

Hugo Ricardo Navarro-Contreras  <https://orcid.org/0000-0003-0333-0024>

REFERENCES

- [1] J. Alanís, M. C. Rodríguez-Aranda, A. G. Rodríguez, H. J. Ojeda-Galván, M. E. Mendoza, H. R. Navarro-Contreras, *J. Raman Spectrosc.* **2019**, *50*, 102.
- [2] J. Alanís, H. J. Ojeda-Galván, M. C. Rodríguez-Aranda, A. G. Rodríguez, H. Moreno García, J. Íñiguez, M. E. Mendoza, H. R. Navarro-Contreras, *Phys. Rev. B* **2019**, *100*, 54110.
- [3] G. Shabbir, S. Kojima, *J. Phys. D Appl. Phys.* **2003**, *36*, 1036.
- [4] D. Chen, J. Ye, *Chem. Mater.* **2009**, *21*, 2327.
- [5] A. Sakai, T. Kanno, K. Takahashi, A. Omote, H. Adachi, Y. Yamada, *J. Am. Ceram. Soc.* **2012**, *95*, 1750.
- [6] A. Sakai, K. Takahashi, T. Kanno, H. Adachi, *IOP Conf. Ser.: Mater. Sci. Eng.* **2011**, *18*, 142011.
- [7] T. D. Sparks, P. A. Fuierer, D. R. Clarke, *J. Am. Ceram. Soc.* **2010**, *93*(4), 1136.
- [8] F. Lichtenberg, A. Herrnberger, K. Wiedenmann, J. Mannhart, *Prog. Solid State Chem.* **2001**, *29*, 1.
- [9] F. Lichtenberg, A. Herrnberger, K. Wiedenmann, *Prog. Solid State Chem.* **2008**, *36*, 253.
- [10] W. Kobayashi, Y. Hayashi, M. Matsushita, Y. Yamamoto, I. Terasaki, A. Nakao, H. Nakao, Y. Murakami, Y. Moritomo, H. Yamauchi, M. Karppinen, *Phys. Rev. B* **2011**, *84*, 085118.
- [11] S. Mukhopadhyay, L. Lindsay, D. J. Singh, *Sci. Rep.* **2016**, *6*, 37076.
- [12] P. Daniels, R. Tamazyan, C. A. Kuntscher, M. Dressel, F. Lichtenberg, S. van Smaalen, *Acta Crystallogr. Sect. B Struct. Sci.* **2002**, *58*, 970.
- [13] G. Kresse, J. Furthmüller, *Phys. Rev. B* **1996**, *54*, 11169.
- [14] G. I. Csonka, J. P. Perdew, A. Ruzsinszky, P. H. T. Philipsen, S. Lebègue, J. Paier, O. A. Vydrov, J. G. Ángyán, *Phys. Review B* **2009**, *79*, 155107.
- [15] G. Kresse, D. Joubert, *Phys. Rev. B* **1999**, *59*, 1758.
- [16] H. J. Monkhorst, J. D. Pack, *Phys. Rev. B* **1977**, *16*, 1748.
- [17] E. Zolotoyabko, *J. Appl. Cryst.* **2009**, *42*, 513.
- [18] F. X. Zhang, J. Lian, U. Becker, R. C. Ewing, L. M. Wang, J. Hu, S. K. Saxena, *J. Solid State Chem.* **2007**, *180*, 571.
- [19] I. Loa, K. Syassen, X. Wang, F. Lichtenberg, M. Hanfland, C. A. Kuntscher, *Phys. Rev. B* **2004**, *69*, 224105.
- [20] C. A. Kuntscher, S. Gerhold, N. Nücker, T. R. Cummins, D.-H. Lu, S. Schuppler, C. S. Gopinath, F. Lichtenberg, J. Mannhart, K.-P. Bohnen, *Phys. Rev. B* **2000**, *61*, 1876.
- [21] C. A. Kuntscher, S. Schuppler, P. Haas, B. Gorshunov, M. Dressel, M. Grioni, F. Lichtenberg, A. Herrnberger, F. Mayr, J. Mannhart, *Phys. Rev. Lett.* **2002**, *89*, 236403.
- [22] H. Winter, S. Schuppler, C. A. Kuntscher, *J. Phys. Condens. Matter* **2000**, *12*, 1735.
- [23] J. Nisar, B. Pathak, R. Ahuja, *Appl. Phys. Lett.* **2012**, *100*, 181903.
- [24] V. Bobnar, P. Lunkenheimer, J. Hemberger, A. Loidl, F. Lichtenberg, J. Mannhart, *Phys. Rev. B* **2002**, *65*, 155115.
- [25] M. Kumar, U. Chandra, G. Parthasarathy, *Mater. Lett.* **2006**, *60*, 2066.
- [26] Y. Nezu, Y. Q. Zhang, C. Chen, Y. Ikuhara, H. Ohta, *J. Appl. Phys.* **2017**, *122*, 135305.
- [27] K. Ito, T. Horikoshi, K. Ohi, *Ferroelectrics* **1997**, *203*, 201.
- [28] I. Kawanishi, H. Fujimori, N. Matsushita, *Trans. Mater. Res. Soc. Japan* **2017**, *42*, 145.
- [29] E. Buixaderas, S. Kamba, J. Petzelt, *J. Phys. Condens. Matter* **2001**, *13*, 2823.
- [30] E. Kroumova, M. I. Aroyo, J. M. Perez-Mato, A. Kirov, C. Capillas, S. Ivantchev, H. Wondratschek, *Phase Transitions* **2003**, *76*, 155.
- [31] P. Colomban, F. Romain, A. Neiman, I. Animitsa, *Solid State Ion.* **2001**, *145*, 339.
- [32] W. Hayes, R. Loudon, *Scattering of Light by Crystals*, Wiley, New York **1978** 360.
- [33] S. Kojima, S. Tsukada, Y. Akishige, *Ferroelectrics* **2017**, *512*, 20.
- [34] G. Shabbir, Y. Akishige, S. Kojima, *Sci. Technol. Adv. Mater.* **2005**, *6*, 656.
- [35] P. G. Klemens, *Phys. Rev. B* **1966**, *148*, 845.
- [36] J. Menéndez, M. Cardona, *Phys. Rev. B* **1984**, *29*, 2051.

- [37] M. C. Rodríguez-Aranda, A. G. Rodríguez-Vázquez, U. Salazar-Kuri, M. E. Mendoza, H. R. Navarro-Contreras, *J. Appl. Phys.* **2018**, 123, 084101.
- [38] X. Li, H. Cai, L. Ding, X. Dou, W. Zhang, *J. Alloys Compd.* **2012**, 541, 36.
- [39] C. Li, H. Xiang, Y. Qin, L. Fang, *J. Adv. Dielectr.* **2017**, 7, 1750013.
- [40] A. Hushur, Y. Akishige, S. Kojima, *Mater. Sci. Eng., B* **2005**, 120, 45.
- [41] H. Fujimori, I. Kawanishi, N. Matsushita, *Trans. Mater. Res. Soc. Japan* **2018**, 43, 7.
- [42] T. Chen, R. Liang, K. Jiang, Z. Hu, Z. Zhou, X. Dong, *J. Am. Ceram. Soc.* **2017**, 100, 2397.
- [43] N. Ishizawa, K. Ninomiya, J. Wang, *Acta Crystallogr.* **2019**, B75, 257.

SUPPORTING INFORMATION

Additional supporting information may be found online in the Supporting Information section at the end of this article.

How to cite this article: Ojeda-Galván HJ, Rodríguez-Aranda MC, Rodríguez ÁG, et al. Structural and Raman study of the thermoelectric solid solution $\text{Sr}_{1.9}\text{La}_{0.1}\text{Nb}_2\text{O}_7$. *J Raman Spectrosc.* 2020;1–13. <https://doi.org/10.1002/jrs.6032>